Available online at www.sciencedirect.com
ScienceDirect
Journal of Sound and Vibration 297 (2006) 704–726
JOURNAL OF SOUND AND VIBRATION
www.elsevier.com/locate/jsvi

Computation of modal stress resultants for completely free vibrating plates by LSFD method

W.X. Wu[a], C. Shu[a,*], C.M. Wang[b]

[a]Department of Mechanical Engineering, National University of Singapore 10 Kent Ridge Crescent 117576, Singapore
[b]Engineering Science Programme, Department of Civil Engineering, National University of Singapore, 10 Kent Ridge Crescent 117576, Singapore

Received 27 May 2005; received in revised form 10 March 2006; accepted 21 April 2006
Available online 27 June 2006

Abstract

When the Ritz method, the Galerkin's method and the finite element method are adopted for the vibration analysis of thin plates, the natural frequencies and mode shapes can normally be obtained accurately. However, the corresponding modal stress resultants usually violate the natural boundary conditions at the free edges and contain erroneous oscillations. Therefore, the accuracy of modal stress resultants obtained by such methods is uncertain. In this study, a meshfree least squares-based finite difference method (LSFD) is proposed for evaluating the vibration solutions of completely free plates. Examples treated include circular plates, elliptical plates, lifting-tab shaped plates and 45° right triangular plates. It will be shown that the LSFD method not only furnishes accurate natural frequencies, but also yields excellent modal stress resultants that satisfy the natural boundary conditions of the free edges and are smooth in their distribution over the plate domain.

1. Introduction

Not known to many structural engineers, a pontoon-type, very large floating structure (VLFS) may be modeled as a giant plate with free edges [1]. As these VLFSs are relatively flexible in the sea, hydroelastic analyses have to be performed so as to determine the dynamic responses of the VLFSs under the action of waves. When adopting the frequency domain approach for the hydroelastic analysis, it is necessary to obtain very accurate frequency values, mode shapes and modal stress resultants up to very high number of modes. Unfortunately, accurate distributions of stress resultants for such VLFSs modeled as freely vibrating plates are often very difficult to obtain either analytically or numerically, although accurate natural frequencies and mode shapes of vibrating plates can be obtained by using the finite element method.

For completely free circular plates, exact solutions for natural frequencies were obtained in terms of Bessel functions by Itao and Crandall [2] and Leissa [3]. Besides, numerical solutions for natural frequencies were

*Corresponding author. Tel.: +65 68746476; fax: +65 67791459.
E-mail address: mpeshuc@nus.edu.sg (C. Shu).

0022-460X/$ - see front matter
doi:10.1016/j.jsv.2006.04.019

obtained by Sato [4], Narita [5], Kim and Dickinson [6] and Lam et al. [7]. In addition, the numerical solutions for natural frequencies for completely free annular plates were presented in Leissa's book [3].

For completely free elliptical plates, Sato [4] obtained the solution of the equation of motion in terms of Mathieu functions and modified Mathieu functions and gave the natural frequency values for the first five doubly symmetric modes. The numerical solutions for natural frequencies were also obtained by Beres [8], Narita [5] and Lam et al. [7] using the Ritz method. The mode shapes for the first six modes of a completely free elliptical plate were presented by Lam et al. [7]. The experimental results for relative frequencies and nodal patterns of a brass elliptical plate were presented in Leissa's book [3].

Apart from circular and elliptical plates, vibration solutions for square and rectangular plates with free edges have been obtained. In Leissa's book [3], many numerical and experimental results of frequency parameters, nodal patterns and mode shapes for the completely free square and rectangular plates are given. More recently, Gorman [9,10], Li [11] and Oosterhout et al. [12] solved the vibration problem of square and rectangular plates with free edges using various numerical techniques such as the superposition method, the reciprocal theorem method, and the Ritz method.

To date, relatively little results can be found in the literature for the vibration of completely free plates with other more general shapes. These completely free vibrating plate results include experimentally obtained relative frequencies and nodal patterns for 45° right triangular brass plates [3,13], several nodal patterns for equilateral triangular plates, regular pentagonal, hexagonal and octagonal plates, and a semicircular plate [3,14].

All foregoing analytical and numerical studies were carried out by using the classical thin-plate theory. For thick plates, the Mindlin plate theory must be used to incorporate the significant effects of transverse shear deformation and rotary inertia on the vibration solutions. Irie et al. [15] derived exact solutions for the natural frequencies of circular Mindlin plates. Liew et al. [16] presented the frequency parameters for the completely free elliptical Mindlin plates using the Ritz method. Wang et al. [17] presented exact solutions for frequencies, as well as mode shapes and stress resultants for completely free circular Mindlin plates.

Based on the literature survey, we find that the accurate distributions of stress resultants obtained based on the classical thin plate theory for completely free circular and elliptical plates are not available in the literature. It was also revealed that for rectangular plates with free edges, the stress resultants obtained by the classical thin-plate theory and using the Galerkin's method, the Ritz method and the finite-element method do not strictly satisfy the natural boundary conditions and they often contain erroneous "oscillations" [18,19]. Therefore, the accuracy of the stress resultants obtained by using these methods is uncertain.

In this paper, a least-squares-based finite difference method (LSFD) is proposed to obtain not only accurate frequencies and mode shapes, but also accurate modal stress resultants for the completely free vibrating plates based on the classical thin-plate theory. Sample results are given for circular plates, elliptical plates, lifting-tab shaped plates and 45° right triangular plates. Other than the Galerkin's method, the Ritz method and the finite-element method which solve the weak form of system equations, LSFD is a meshfree method which solves the strong form of system equations. Using LSFD, the derivatives of a function in the governing differential equation (PDE) and the PDEs for boundary conditions are directly discretized so that a system of algebraic equations can be derived and then solved by using a common solver. Therefore, in this solution procedure, the natural boundary conditions are imposed and therefore are satisfied a priori, and one can be sure that a well-converged solution is accurate. The second advantage of LSFD method, when comparing with the traditional finite-difference method (FDM) and differential quadrature method (DQM), is that problems with generally shaped two-dimensional (2D) domains can be easily solved by utilizing randomly distributed points in the domains, without any complexity of coordinate transformation or domain decomposition.

In the classical thin plate theory, the governing equation for free vibration of plates is a fourth-order PDE and the boundary conditions for free edges are given by one second-order and one third-order PDEs. It is a challenging task to solve high-order PDEs with multiple boundary conditions by using numerical methods. The difficulties mainly lie in the accurate approximation of high-order derivatives and the effective implementation of multiple boundary conditions. In the present study, these difficulties are overcome by using a chain rule of discretization. For example, a fourth-order derivative can be expressed as a second-order derivative of another second-order derivative of the function, such as $\partial^4 W/\partial x^4 = \partial^2(\partial^2 W/\partial x^2)/\partial x^2$, then it can be discretized in two or three steps where the order of derivatives is reduced gradually. This is done with the view to obtain sufficient accuracy for discretization of the high-order derivatives in the PDEs.

By using LSFD method, the multiple boundary conditions are implemented by solving the system of discretized equations of boundary conditions, and expressing the function values at boundary points and a layer of interior points near the boundary in terms of the function values at other interior points. The final eigenvalue equations are derived by substituting above expressions into the fully discretized governing equations. The validity of LSFD method is confirmed by comparing the LSFD results with available data in the literature, by the convergence study of the LSFD results, by assessing the satisfaction of the natural boundary conditions and by the smoothness of the stress resultant distributions. In the selection of plate problems for this purpose, we chose circular and elliptical plates because (a) there are exact analytical solutions for natural frequencies of circular plates which form a reference to assess the performance of the LFSD method and (b) circular and elliptical plates are common plate shapes which engineers would like to use for VLFSs. We also choose a lifting-tab shaped plate (a shape crafted by the authors to represent an arbitrarily shaped plate) and a 45° right triangular plate to demonstrate the capability of the LSFD method in solving problems with complex domain shapes. Owing to length limitation, we shall only present LFSD results for the stress resultant distributions for the fundamental vibration mode of each plate shape. These results should serve as important data for the engineers in their development of software package for the hydroelastic analysis of VLFSs.

2. Least squares-based finite difference (LSFD) method

2.1. Basic LSFD formulations

In this section, a summary of the methodology of LSFD method is presented. The detailed description of the method was earlier given by Ding et al. [20].

For a continuous, differentiable function $W(x,y)$ in a 2D domain, in which a set of points with indices $i = 1,\ldots,N_t$ are distributed randomly, the Taylor series expansion in Δ-form gives:

$$\Delta W_{ij} = \Delta x_{ij}\frac{\partial W_i}{\partial x} + \Delta y_{ij}\frac{\partial W_i}{\partial y} + \frac{\Delta x_{ij}^2}{2}\frac{\partial^2 W_i}{\partial x^2} + \frac{\Delta y_{ij}^2}{2}\frac{\partial^2 W_i}{\partial y^2} + \Delta x_{ij}\Delta y_{ij}\frac{\partial^2 W_i}{\partial x\partial y} + \frac{\Delta x_{ij}^3}{6}\frac{\partial^3 W_i}{\partial x^3} + \frac{\Delta y_{ij}^3}{6}\frac{\partial^3 W_i}{\partial y^3} + \frac{\Delta x_{ij}^2\Delta y_{ij}}{2}\frac{\partial^3 W_i}{\partial x^2\partial y} + \frac{\Delta x_{ij}\Delta y_{ij}^2}{2}\frac{\partial^3 W_i}{\partial x\partial y^2} + O(\Delta^4), \tag{1}$$

where $\Delta W_{ij} = W_{ij} - W_i$, $\Delta x_{ij} = x_{ij} - x_i$, $\Delta y_{ij} = y_{ij} - y_i$; (x_i, y_i) are the coordinates of the point i, (x_{ij}, y_{ij}) the coordinates of a neighboring point ij (hereafter we call it a supporting point) of the point i, W_i the function value at the point i, W_{ij} the function value at the point ij, $\partial W_i/\partial x$ and $\partial W_i/\partial y$, etc. the derivative values of function $W(x, y)$ evaluated at the point i. Δ in the truncation error term, $O(\Delta^4)$, is a measurement of the mean distance from the set of supporting points ij to the point i, for $j = 1,2,\ldots,m$.

If we apply Eq. (1) to approximate function values W_{ij} at a number of supporting points ij ($j = 1,2,\ldots,m$; $m>9$) of the point i, and drop the truncation errors $O(\Delta^4)$, we can have a system of equations in a compact form:

$$\Delta\mathbf{W}_i = \mathbf{S}_i\,\mathrm{d}\mathbf{W}_i, \tag{2}$$

where

$$\Delta\mathbf{W}_i = \begin{bmatrix}\Delta W_{i1} & \Delta W_{i2} & \cdots & \Delta W_{im}\end{bmatrix}^{\mathrm{T}}, \tag{3}$$

$$d\mathbf{W}_i = \begin{bmatrix}\frac{\partial W_i}{\partial x} & \frac{\partial W_i}{\partial y} & \frac{\partial^2 W_i}{\partial x^2} & \frac{\partial^2 W_i}{\partial y^2} & \frac{\partial^2 W_i}{\partial x\partial y} & \frac{\partial^3 W_i}{\partial x^3} & \frac{\partial^3 W_i}{\partial y^3} & \frac{\partial^3 W_i}{\partial x^2\partial y} & \frac{\partial^3 W_i}{\partial x\partial y^2}\end{bmatrix}^{\mathrm{T}}, \tag{4}$$

$$\mathbf{S}_i = \begin{bmatrix} \Delta x_{i1} & \Delta y_{i1} & \frac{\Delta x_{i1}^2}{2} & \frac{\Delta y_{i1}^2}{2} & \Delta x_{i1}\Delta y_{i1} & \frac{\Delta x_{i1}^3}{6} & \frac{\Delta y_{i1}^3}{6} & \frac{\Delta x_{i1}^2 \Delta y_{i1}}{2} & \frac{\Delta x_{i1} \Delta y_{i1}^2}{2} \\ \Delta x_{i2} & \Delta y_{i2} & \frac{\Delta x_{i2}^2}{2} & \frac{\Delta y_{i2}^2}{2} & \Delta x_{i2}\Delta y_{i2} & \frac{\Delta x_{i2}^3}{6} & \frac{\Delta y_{i2}^3}{6} & \frac{\Delta x_{i2}^2 \Delta y_{i2}}{2} & \frac{\Delta x_{i2} \Delta y_{i2}^2}{2} \\ \vdots & \vdots & \vdots & \vdots & \vdots & \vdots & \vdots & \vdots & \vdots \\ \Delta x_{im} & \Delta y_{im} & \frac{\Delta x_{im}^2}{2} & \frac{\Delta y_{im}^2}{2} & \Delta x_{im}\Delta y_{im} & \frac{\Delta x_{im}^3}{6} & \frac{\Delta y_{im}^3}{6} & \frac{\Delta x_{im}^2 \Delta y_{im}}{2} & \frac{\Delta x_{im} \Delta y_{im}^2}{2} \end{bmatrix}. \tag{5}$$

Now, we define a matrix

$$\mathbf{D}_i = \mathrm{diag}\left(d_i, d_i, d_i^2, d_i^2, d_i^2, d_i^3, d_i^3, d_i^3, d_i^3\right), \tag{6}$$

where d_i is the radius of the supporting region of the point i, then from Eq. (2) we have

$$\Delta \mathbf{W}_i = \bar{\mathbf{S}}_i \, \mathrm{d}\bar{\mathbf{W}}_i, \tag{7}$$

where

$$\bar{\mathbf{S}}_i = \mathbf{S}_i \mathbf{D}_i^{-1}, \ \mathrm{d}\bar{\mathbf{W}}_i = \mathbf{D}_i \, \mathrm{d}\mathbf{W}_i. \tag{8}$$

In Eq. (7), the number of equations is greater than the number of unknowns (i.e. the derivatives given in expression (4)), i.e. $m > 9$. This is done purposely because the matrices $\mathbf{S}_i$ are often singular or ill-conditioned at some points i in the domain Ω when $m = 9$. We can use the least-squares technique to solve for $\mathrm{d}\bar{\mathbf{W}}_i$ from Eq. (7). That is, pre-multiplying the matrix $\bar{\mathbf{S}}_i^{\mathrm{T}}$ to the two sides of Eq. (7), we have

$$\bar{\mathbf{S}}_i^{\mathrm{T}} \Delta \mathbf{W}_i = \bar{\mathbf{S}}_i^{\mathrm{T}} \bar{\mathbf{S}}_i \, \mathrm{d}\bar{\mathbf{W}}_i. \tag{9}$$

The dimensions of matrices $\bar{\mathbf{S}}_i$ and $\bar{\mathbf{S}}_i^{\mathrm{T}}$ are $m \times 9$ and $9 \times m$, respectively, hence the dimension of matrix $\bar{\mathbf{S}}_i^{\mathrm{T}} \bar{\mathbf{S}}_i$ is 9×9. m is taken big enough to ensure the matrices $\bar{\mathbf{S}}_i^{\mathrm{T}} \bar{\mathbf{S}}_i$ are non-singular at all points i in Ω. Therefore, from Eq. (9), we get

$$\mathrm{d}\bar{\mathbf{W}}_i = \left(\bar{\mathbf{S}}_i^{\mathrm{T}} \bar{\mathbf{S}}_i\right)^{-1} \bar{\mathbf{S}}_i^{\mathrm{T}} \Delta \mathbf{W}_i. \tag{10}$$

Moreover, in order to reflect the fact that a supporting point closer to the node i has more influence on the function value at the node i, a weighting function matrix is introduced in Eq. (10) so that

$$\mathrm{d}\bar{\mathbf{W}}_i = \left(\bar{\mathbf{S}}_i^{\mathrm{T}} \mathbf{V}_i \bar{\mathbf{S}}_i\right)^{-1} \bar{\mathbf{S}}_i^{\mathrm{T}} \mathbf{V}_i \Delta \mathbf{W}_i, \tag{11}$$

where

$$\mathbf{V}_i = \mathrm{diag}(V_{i1}, V_{i2}, \cdots, V_{im}) \tag{12}$$

in which the weighting functions are taken as

$$V_{ij} = \sqrt{4/\pi}\left(1 - \bar{r}_{ij}^2\right)^4 \tag{13}$$

and

$$\bar{r}_{ij} = \sqrt{\Delta x_{ij}^2 + \Delta y_{ij}^2}/d_i.$$

The final LSFD formulations can be derived from Eqs. (8) and (11) as

$$\mathrm{d}\mathbf{W}_i = \mathbf{D}_i^{-1}\left(\bar{\mathbf{S}}_i^{\mathrm{T}} \mathbf{V}_i \bar{\mathbf{S}}_i\right)^{-1} \bar{\mathbf{S}}_i^{\mathrm{T}} \mathbf{V}_i \Delta \mathbf{W}_i. \tag{14}$$

In order to simplify this formulation, we can define matrices, each of which is associated with a point i, as

$$\mathbf{T}^i = \mathbf{D}_i^{-1}\left(\bar{\mathbf{S}}_i^{\mathrm{T}} \mathbf{V}_i \bar{\mathbf{S}}_i\right)^{-1}\left(\bar{\mathbf{S}}_i^{\mathrm{T}} \mathbf{V}_i\right), \tag{15}$$

then formulation (14) can be simply rewritten as

$$\mathrm{d}\mathbf{W}_i = \mathbf{T}^i \Delta \mathbf{W}_i, \tag{F-9}$$

where $\Delta\mathbf{W}_i$ and $\mathrm{d}\mathbf{W}_i$ are vectors given by expressions (3) and (4), respectively, and $\mathrm{T}^i \in R^{9\times m}$. Eq. (F-9) shows that a derivative of the function $W(x,y)$ at a point i can be approximated by a linear combination of the function values at the point i and a set of its supporting points ij.

From above process, it is seen that the LSFD formulation (F-9) is derived by using the 2D Taylor series expansion with first nine truncated terms. We can also derive higher-order LSFD schemes which approximate derivatives of a function with higher accuracy by using the 2D Taylor series expansions with more truncated terms. For convenience of citation, we denote by (F-N) the LSFD formulation, in the same form as (F-9), which is derived by using the 2D Taylor series expansion with first N truncated terms.

2.2. LSFD formulations for derivative approximation at boundary in terms of local nt-coordinate system

If the boundary conditions are given in terms of the derivatives of function to n and/or t, where n, t are the local coordinates along the outer normal and tangential directions, respectively, at the boundary $\mathbf{\Gamma}$ (see Fig. 1), eg $\partial W/\partial n = 0$ at $\mathbf{\Gamma}$, then we can use LSFD method to derive the formulations to approximate the derivatives of function in n- and t-local directions at a boundary point. The use of these formulations to discretize the PDEs for boundary conditions is more convenient than that of (F-N) which is in terms of global xy-coordinates.

The procedure for deriving such formulations is similar to that of Eqs. (1)–(F-9). At a boundary point i with the local nt-coordinate system (see Fig. 1) and supporting points $ij(j = 1,2,\ldots,m$; and $m>9)$, the Taylor series expansion can be written as

$$\begin{aligned}\Delta W_{ij} = {} & \Delta n_{ij}\frac{\partial W_i}{\partial n} + \Delta t_{ij}\frac{\partial W_i}{\partial t} + \frac{\Delta n_{ij}^2}{2}\frac{\partial^2 W_i}{\partial n^2} + \frac{\Delta t_{ij}^2}{2}\frac{\partial^2 W_i}{\partial t^2} + \Delta n_{ij}\Delta t_{ij}\frac{\partial^2 W_i}{\partial n\partial t} \\ & + \frac{\Delta n_{ij}^3}{6}\frac{\partial^3 W_i}{\partial n^3} + \frac{\Delta t_{ij}^3}{6}\frac{\partial^3 W_i}{\partial t^3} + \frac{\Delta n_{ij}^2\Delta t_{ij}}{2}\frac{\partial^3 W_i}{\partial n^2\partial t} + \frac{\Delta n_{ij}\Delta t_{ij}^2}{2}\frac{\partial^3 W_i}{\partial n\partial t^2} + O(\Delta^4),\end{aligned} \tag{16}$$

where

$$\Delta W_{ij} = W_{ij} - W_i, \tag{17}$$

$$\begin{cases}\Delta n_{ij} = n_{ij} - n_i = \Delta x_{ij}\ \cos\ \theta_i + \Delta y_{ij}\sin\theta_i, \\ \Delta t_{ij} = t_{ij} - t_i = -\Delta x_{ij}\ \sin\ \theta_i + \Delta y_{ij}\cos\theta_i.\end{cases} \tag{18}$$

The relations given by Eq. (18) can be easily verified from Fig. 1.

After a similar process, we can arrive at

$$\mathrm{d}\mathbf{W}_i = \tilde{\mathbf{T}}^i\Delta\mathbf{W}_i, \tag{F-9a}$$

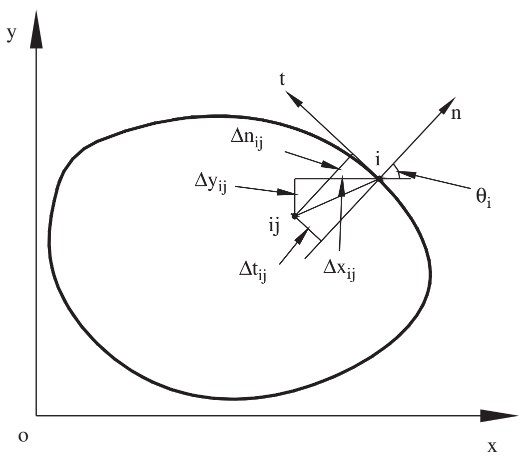

Fig. 1. Local nt-coordinate system.

where

$$\mathrm{d}\mathbf{W}_i = \begin{bmatrix} \frac{\partial W_i}{\partial n} & \frac{\partial W_i}{\partial t} & \frac{\partial^2 W_i}{\partial n^2} & \frac{\partial^2 W_i}{\partial t^2} & \frac{\partial^2 W_i}{\partial n \partial t} & \frac{\partial^3 W_i}{\partial n^3} & \frac{\partial^3 W_i}{\partial t^3} & \frac{\partial^3 W_i}{\partial n^2 \partial t} & \frac{\partial^3 W_i}{\partial n \partial t^2} \end{bmatrix}^{\mathrm{T}}, \tag{19}$$

$$\Delta\mathbf{W}_i = \begin{bmatrix} \Delta W_{i1} & \Delta W_{i2} & \cdots & \Delta W_{im} \end{bmatrix}^{\mathrm{T}}, \tag{20}$$

$$\tilde{\boldsymbol{T}}^i = \mathbf{D}_i^{-1}\left(\bar{\mathbf{S}}_i^{\mathrm{T}}\mathbf{V}_i\bar{\mathbf{S}}_i\right)^{-1}\left(\bar{\mathbf{S}}_i^{\mathrm{T}}\mathbf{V}_i\right) \quad \tilde{\mathbf{T}}^i \in R^{9\times m}, \tag{21}$$

$$\boldsymbol{S}_i = \begin{bmatrix} \Delta n_{i1} & \Delta t_{i1} & \frac{\Delta n_{i1}^2}{2} & \frac{\Delta t_{i1}^2}{2} & \Delta n_{i1}\Delta t_{i1} & \frac{\Delta n_{i1}^3}{6} & \frac{\Delta t_{i1}^3}{6} & \frac{\Delta n_{i1}^2 \Delta t_{i1}}{2} & \frac{\Delta n_{i1}\Delta t_{i1}^2}{2} \\ \Delta n_{i2} & \Delta t_{i2} & \frac{\Delta n_{i2}^2}{2} & \frac{\Delta t_{i2}^2}{2} & \Delta n_{i2}\Delta t_{i2} & \frac{\Delta n_{i2}^3}{6} & \frac{\Delta t_{i2}^3}{6} & \frac{\Delta n_{i2}^2 \Delta t_{i2}}{2} & \frac{\Delta n_{i2}\Delta t_{i2}^2}{2} \\ \vdots & \vdots & \vdots & \vdots & \vdots & \vdots & \vdots & \vdots & \vdots \\ \Delta n_{im} & \Delta t_{im} & \frac{\Delta n_{im}^2}{2} & \frac{\Delta t_{im}^2}{2} & \Delta n_{im}\Delta t_{im} & \frac{\Delta n_{im}^3}{6} & \frac{\Delta t_{im}^3}{6} & \frac{\Delta n_{im}^2 \Delta t_{im}}{2} & \frac{\Delta n_{im}\Delta t_{im}^2}{2} \end{bmatrix}. \tag{22}$$

The matrices $\mathbf{D}_i$, $\bar{\mathbf{S}}_i$ and $\mathbf{V}_i$ are in the same forms as those given in Eqs. (6), (8) and (12), respectively. Analogous to the notation (F-N), we use (F-Na) to denote the derivative approximating formulation in the same form as (F-9a) but derived by using the 2D Taylor series expansion with first N truncated terms.

2.3. LSFD formulations for $\nabla^2 W_i$ and $\nabla^2(\nabla^2 W_i)$—chain rule of discretization

In view of the Laplacian operator in a dimensionless form

$$\nabla^2 = \frac{\partial^2}{\partial X^2} + \frac{\partial^2}{\partial Y^2} \tag{23}$$

and using formulation (F-N), we can derive following discretization:

$$\nabla^2 W_i = \sum_{j=1}^{m}\left(T_{3,j}^i + T_{4,j}^i\right)\Delta W_{ij} = \sum_{j=1}^{m}\left(T_{3,j}^i + T_{4,j}^i\right)W_{ij} + \left\{-\sum_{j=1}^{m}\left(T_{3,j}^i + T_{4,j}^i\right)\right\}W_i. \tag{24}$$

We define a vector c^i which is associated with point i by giving its elements as

$$c_j^i = T_{3,j}^i + T_{4,j}^i \quad \text{for } j = 1, 2, \cdots, m \tag{25}$$

then Eq. (24) can be simplified as

$$\nabla^2 W_i = \sum_{j=1}^{m} c_j^i \Delta W_{ij} = \sum_{j=1}^{m} c_j^i W_{ij} + \left(-\sum_{j=1}^{m} c_j^i\right)W_i. \tag{26}$$

Based on the classical thin plate theory, the governing equation for the free vibration of a plate is given by [21]

$$\nabla^2\left(\nabla^2 W\right) = \Omega^2 W. \tag{27}$$

We can treat $\nabla^2 \mathrm{W}_i$ as the value of a function at point (x_i, y_i). Following Eq. (26), we can derive

$$\nabla^2\left(\nabla^2 W_i\right) = \sum_{j=1}^{m} c_j^i \nabla^2 W_{ij} + \left(-\sum_{j=1}^{m} c_j^i\right)\nabla^2 W_i \tag{28-1}$$

$$= \sum_{j=1}^{m} c_j^i \left\{ \sum_{k=1}^{m} c_k^{ij} W_{ijk} + \left(-\sum_{k=1}^{m} c_k^{ij} \right) W_{ij} \right\} + \left(-\sum_{j=1}^{m} c_j^i \right) \left\{ \sum_{j=1}^{m} c_j^i W_{ij} + \left(-\sum_{j=1}^{m} c_j^i \right) W_i \right\}$$

$$= \sum_{j=1}^{m} \sum_{k=1}^{m} c_j^i c_k^{ij} W_{ijk} + \sum_{j=1}^{m} c_j^i \left(-\sum_{k=1}^{m} c_k^{ij} \right) W_{ij} + \left(-\sum_{j=1}^{m} c_j^i \right) \sum_{j=1}^{m} c_j^i W_{ij} + \left(-\sum_{j=1}^{m} c_j^i \right)^2 W_i, \tag{28-2}$$

where W_{ijk} is to be understood as the function value at the point ijk, and the subscript ijk refers to the index of the kth supporting point of the point ij. So the fully descritized form of Eq. (27) can be written as

$$\sum_{j=1}^{m} \sum_{k=1}^{m} c_j^i c_k^{ij} W_{ijk} + \sum_{j=1}^{m} c_j^i \left(-\sum_{k=1}^{m} c_k^{ij} \right) W_{ij} + \left(-\sum_{j=1}^{m} c_j^i \right) \sum_{j=1}^{m} c_j^i W_{ij} + \left(-\sum_{j=1}^{m} c_j^i \right)^2 W_i = \Omega^2 W_i. \tag{29}$$

3. Free vibration analysis of completely free plates

3.1. Problem definition

The governing equation of a thin isotropic plate undergoing harmonic free vibration is given in Eq. (27), in which $W = W(X, Y)$ is the mode function of plate deflection; $X = x/a, Y = y/a$ are dimensionless Cartesian coordinates in the plane of the mid-surface of the plate; a is a characteristic dimension of the plate in the xy-plane. Ω is the frequency parameter of a principal mode of plate vibration and is related to the angular frequency ω(rad/s) in the form

$$\Omega = \omega a^2 \sqrt{\frac{\rho h}{D}}, \tag{30}$$

where ρ is the density of the plate material, h the plate thickness; and

$$D = \frac{Eh^3}{12(1 - v^2)} \tag{31}$$

the flexural rigidity of the plate; E and v being, respectively, Young's modulus and Poisson's ratio of the plate material.

The boundary conditions for a free edge are given by [21]

$$\frac{\partial^2 W}{\partial n^2} + v \frac{\partial^2 W}{\partial t^2} = 0, \tag{32a}$$

$$\frac{\partial}{\partial n} \left(\nabla^2 W \right) + (1 - v) \frac{\partial}{\partial s} \left(\frac{\partial^2 W}{\partial n \partial t} \right) = 0. \tag{32b}$$

In Eq. (32b), $\partial/\partial s$ denotes the differentiation along the boundary curve. For a straight boundary line, $\partial/\partial s = \partial/\partial t$. Physically, Eq. (32a) implies that the normal bending moment at a free edge is equal to zero, while Eq. (32b) implies that the normal effective shear force at a free edge is zero.

Apart from the accurate results for frequency parameters and mode shapes, we shall also obtain the accurate results for stress resultants in the completely free vibrating plates. The stress resultants are computed by using following formulations [21]:

$$M_x = -D \left(\frac{\partial^2 W}{\partial x^2} + v \frac{\partial^2 W}{\partial y^2} \right) \quad M_y = -D \left(\frac{\partial^2 W}{\partial y^2} + v \frac{\partial^2 W}{\partial x^2} \right), \tag{33a}$$

$$M_{xy} = D(1 - v) \frac{\partial^2 W}{\partial x \partial y}, \tag{33b}$$

$$Q_x = -D\frac{\partial}{\partial x}\left(\nabla^2 W\right) \quad Q_y = -D\frac{\partial}{\partial y}\left(\nabla^2 W\right), \tag{33c}$$

$$V_n = Q_n - \frac{\partial M_{nt}}{\partial s}, \tag{33d}$$

$$M_{x'} = M_x \cos^2\alpha + M_y \sin^2\alpha - 2M_{xy} \sin\alpha \cos\alpha, \tag{33e}$$

$$M_{x'y'} = M_{xy}\left(\cos^2\alpha - \sin^2\alpha\right) + \left(M_x - M_y\right) \sin\alpha \cos\alpha, \tag{33f}$$

$$Q_{x'} = Q_x \cos\alpha + Q_y \sin\alpha. \tag{33g}$$

x' denotes the direction which makes an angle α with x-axis. By setting $\partial M_{x'}/\partial\alpha = 0$, we get

$$\alpha_1 = \frac{1}{2}\arctan\frac{2M_{xy}}{-M_x + M_y} \quad \alpha_2 = \frac{1}{2}\arctan\frac{2M_{xy}}{-M_x + M_y} + \frac{\pi}{2}. \tag{34a}$$

By back substituting Eq. (34a) into Eq. (33e), we obtain the principal bending moments at a point of interest. By setting $\partial M_{x'y'}/\partial\alpha = 0$, we get

$$\alpha_3 = \frac{1}{2}\arctan\frac{M_x - M_y}{2M_{xy}} \quad \alpha_4 = \frac{1}{2}\arctan\frac{M_x - M_y}{2M_{xy}} + \frac{\pi}{2}. \tag{34b}$$

The back-substitution of Eq. (34b) into Eq. (33f) furnishes the maximum and minimum twisting moments at a point of interest. By setting $\partial Q_{x'}/\partial\alpha = 0$, we get

$$\alpha_5 = \arctan\frac{Q_y}{Q_x}. \tag{34c}$$

The back -substitution of Eq. (34c) into Eq. (33g) yields the maximum absolute shear forces at a point of interest.

3.2. Numerical implementation

3.2.1. Data preparation

In the plate domain, totally N_t nodal points $\left(x_i, y_i\right), i = 1, 2, \cdots, N_\mathrm{t}$ are generated randomly, in which $i = 1,2,\ldots,N_{ii}$ are interior points in the central area of the plate domain, $(N_\mathrm{i} - N_\mathrm{ii}) \equiv N_\mathrm{b}$ points $i = N_\mathrm{ii}+1, N_\mathrm{ii}+2, \cdots, N_\mathrm{i}$ are a layer of interior points near the plate edge, and the rest $(N_\mathrm{t} - N_\mathrm{i}) \equiv N_\mathrm{b}$ points $i = N_\mathrm{i}+1, N_\mathrm{i}+2, \cdots, N_\mathrm{t}$ are boundary points. The data θ_i for boundary points are also given where θ_i is the angle between the positive x-axis and the positive local n-axis at the boundary point i.

Based on the given data, we generate another datafile in which the global indices of m nearest supporting points of each node i $(i = 1, 2, \cdots, N_t)$ are given as $ij(i,j), j = 1, 2, \cdots, m$. The radius d_i of the supporting region associated to each point i is calculated as

$$d_i = \max\left\{\sqrt{\left(x_{ij} - x_i\right)^2 + \left(y_{ij} - y_i\right)^2}\right\} \times 1.2, \quad \text{for } j = 1, 2, \cdots, m, \quad \text{and } i = 1, 2, \cdots, N_t. \tag{35}$$

The matrices $\mathbf{T}^\mathrm{i}$, vectors $\mathbf{c}^i$ $(i = 1, 2, \cdots, N_t)$ and matrices $\tilde{\mathbf{T}}^i$ $(i = N_\mathrm{i}+1, \cdots, N_\mathrm{t})$ are calculated by using Eqs. (15), (25) and (21), respectively.

3.2.2. Discretization of governing equation

As stated in Section 2.3, the governing equation is given by Eq. (27). At each interior point i, where $i = 1, 2, \cdots, N_\mathrm{ii}$, the left-hand side of Eq. (27) can be discretized in two steps as shown in Eqs. (28-1) and (28-2). Finally, the fully discretized form of Eq. (27) can be written as Eq. (29).

3.2.3. Implementation of free edge boundary conditions

Eq. (32a) for one boundary condition on the free edge can be easily discretized at all the boundary points $i = N_{\mathrm{i}}+1, N_{\mathrm{i}}+2, \cdots, N_t$ by using the formulation (F-*N*a) as

$$\sum_{j=1}^{m}\left(\tilde{T}^{i}_{3,j}+v\tilde{T}^{i}_{4,j}\right)\left(W_{ij}-W_i\right)=0 \tag{36a}$$

and Eq. (32b) for another boundary condition on the free edge can be firstly reduced to the form

$$\frac{\partial}{\partial n}\left(\nabla^2 W\right)+(1-v)\frac{\partial}{\partial s}\left[\cos 2\theta\frac{\partial^2 W}{\partial X\partial Y}+\frac{1}{2}\sin 2\theta\left(\frac{\partial^2 W}{\partial Y^2}-\frac{\partial^2 W}{\partial X^2}\right)\right]=0 \tag{a}$$

which can be further reduced, by performing the differentiation $\partial/\partial s$ of the expression in the square brackets, as

$$\frac{\partial}{\partial n}\left[\nabla^2 W_i+(1-v)\frac{\partial^2 W_i}{\partial t^2}\right] + (1-v)\frac{\partial\theta_i}{\partial s}\left[-2\sin 2\theta_i\frac{\partial^2 W_i}{\partial X\partial Y}+\cos 2\theta_i\left(\frac{\partial^2 W_i}{\partial Y^2}-\frac{\partial^2 W_i}{\partial X^2}\right)\right]=0. \tag{b}$$

Eq. (b) is now written as an equation satisfied at a boundary point *i*. Note that the second term of Eq. (b) relates to the curvature of a curved free edge and vanishes for a straight free edge. Eq. (b) can be further discretized as

$$\sum_{j=1}^{m}\tilde{T}^{i}_{1,j}\left[\nabla^2 W_{ij}+(1-v)\frac{\partial^2 W_{ij}}{\partial t^2}\right]+\left(-\sum_{j=1}^{m}\tilde{T}^{i}_{1,j}\right)\left[\nabla^2 W_i+(1-v)\frac{\partial^2 W_i}{\partial t^2}\right] + (1-v)\frac{\partial\theta_i}{\partial s}\left[-2\sin 2\theta_i\frac{\partial^2 W_i}{\partial X\partial Y}+\cos 2\theta_i\left(\frac{\partial^2 W_i}{\partial Y^2}-\frac{\partial^2 W_i}{\partial X^2}\right)\right]=0. \tag{c}$$

The final discretized form of Eq. (32b) can be derived from Eq. (c) as

$$\begin{aligned}&\sum_{j=1}^{m}\sum_{k=1}^{m}\tilde{T}^{i}_{1,j}\left[c^{ij}_{k}+(1-v)\left(\sin^2\theta_i\cdot T^{ij}_{3,k}+\cos^2\theta_i\cdot T^{ij}_{4,k}-\sin 2\theta_i\cdot T^{ij}_{5,k}\right)\right]\left(W_{ijk}-W_{ij}\right)\\&+\left(-\sum_{j=1}^{m}\tilde{T}^{i}_{1,j}\right)\sum_{j=1}^{m}\left[c^{i}_{j}+(1-v)\tilde{T}^{i}_{4,j}\right]\left(W_{ij}-W_i\right)\\&+\frac{(1-v)}{r_i}\sum_{j=1}^{m}\left[-2\sin 2\theta_i\cdot T^{i}_{5,j}+\cos 2\theta_i\cdot\left(T^{i}_{4,j}-T^{i}_{3,j}\right)\right]\left(W_{ij}-W_i\right)=0.\end{aligned} \tag{36b}$$

In Eq. (36b), $r_i = 1/\left(\partial\theta_i/\partial s\right)$ is the radius of curvature of the curved free edge at the boundary point *i*.

Eqs. (36a,b) derived at all the boundary points form an algebraic equation system in which the function values at all discrete points in the domain are taken as unknowns. By remaining the terms involving the function values at all the boundary points and the same number (N_b) of interior points in the neighborhood of the boundary at the left-hand side, and moving all the terms involving the function values at other interior points to the right-hand side, this equation system can be written in a compact form as

$$\mathbf{Bb}=\mathbf{Ca}, \tag{37}$$

where $\mathbf{a}=\left\{W_1 \ \cdots \ W_{N_{ii}}\right\}^{\mathrm{T}}$, $\mathbf{b}=\left\{W_{N_{ii}+1} \ \cdots \ W_{N_i} \ W_{N_i+1} \ \cdots W_{N_t}\right\}^{\mathrm{T}}$. The coefficient matrices $\mathbf{B}$ and $\mathbf{C}$ are of dimensions $2N_b \times N_b$ and $2N_b \times N_{ii}$, respectively. Eq. (37) can be further reduced as

$$\mathbf{b}=\left(\mathbf{B}^{-1}\mathbf{C}\right)\mathbf{a}. \tag{38}$$

By substituting Eq. (38) in the fully discretized governing equation (29) which is derived at the interior points $i = 1, \cdots, N_{ii}$, an equation system can be arrived:

$$\mathbf{A}\mathbf{a} = \Omega^2 \mathbf{a}. \tag{39}$$

the coefficient matrix $\mathbf{A}$ is of the dimension $N_{ii} \times N_{ii}$. The frequency parameters Ω and corresponding mode shapes $\mathbf{a}$ and $\mathbf{b}$ can be derived by calculating the eigenvalues and eigenvectors of the matrix $\mathbf{A}$ and by using Eq. (38).

3.3. Results and discussion

The results presented in this section are aimed to illustrate the numerical accuracy and efficiency of the LSFD method in solving high-order PDEs with multiple boundary conditions. The problem chosen for this purpose is the free vibration of completely free plates including circular and elliptical plates of size $2a \times 2b$, lifting-tab shaped plates and 45° right triangular plates (see Fig. 2). Although the circular plate problem can be solved by using the cylindrical coordinate system, the present formulation and computation are based on the Cartesian coordinate system. In order to show the accuracy of the LSFD solutions, following studies have been carried out: (1) convergence study of the LSFD solutions; (2) comparison studies on the frequency parameters and nodal circle radii obtained using the LSFD solutions with existing data in the literature; (3) assessment on the satisfaction of the natural boundary conditions by the LSFD solutions. Finally, we present the complete set of LSFD results for the mode shapes and stress resultants for the fundamental modes of the considered completely free plates in 3D and contour plots.

3.3.1. Vibration frequencies

The first three modes of these completely free plates correspond to rigid motions. Therefore, we present the numerical results from the 4th mode onwards. LSFD results for frequency parameters of the circular and elliptical plates are given in Table 1. The results, obtained using three mesh sizes, show clearly the convergence behavior of the solution method when the mesh size is increased. For each mesh size, the LSFD formulations (F-*N*) and (F-*N*a) with $N = 14$, 20, 27 and 35 are used in computation. Therefore, the results demonstrate how the accuracy is affected by the derivative approximating formulations for different orders of LSFD schemes. It can be observed that the accuracy of LSFD results is generally improving when the mesh size increases and when the higher-order LSFD formulations are used. Table 1 shows the LSFD solutions for the first six frequency parameters of the completely free circular and elliptical plates, which are in very good agreement with the benchmark data from Lam et al. [7] and other sources.

LSFD results for the first six frequency parameters of the completely free lifting-tab shaped plate and 45° right triangular plate are given in Tables 2 and 3, respectively. For each case, the results are also obtained using three mesh sizes so as to show the convergence behavior of the solution method when the mesh size is increased. For each mesh size, the LSFD formulations (F-*N*) and (F-*N*a) with $N = 14$, 20 and 27 are used in computation. This is done because we have observed that the results in Table 1 for circular and elliptical plates

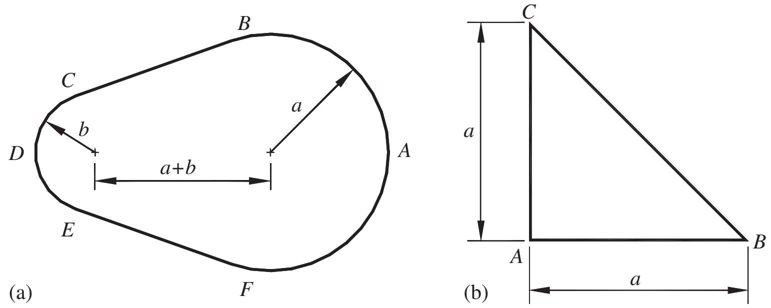

Fig. 2. (a) Lifting-tab shaped plate ($a = 2b$); (b) 45° right triangular plate.

Table 1
LSFD solution for the first six frequencies of completely free circular and elliptic plates ($\Omega = \omega a^2\sqrt{\rho h/D}$, $v = 0.3$)

Method	Mesh	Formulation	Mode sequence					
			4th	5th	6th	7th	8th	9th
Circular plate, $a/b = 1.0$								
LSFD	406	F-14	4.9367	4.9537	8.3257	11.169	11.234	17.659
		F-20	5.3261	5.3301	9.0514	12.092	12.121	20.487
		F-27	5.3631	5.3636	9.0168	12.441	12.454	20.733
		F-35	5.3569	5.3575	8.9809	12.541	12.544	21.043
	1490	F-14	5.2320	5.2357	8.8757	12.021	12.033	19.760
		F-20	5.3579	5.3582	9.0032	12.393	12.400	20.498
		F-27	5.3584	5.3584	9.0031	12.438	12.441	20.478
		F-35	5.3584	5.3584	9.0001	12.436	12.436	20.463
	2468	F-14	5.2802	5.2802	8.9394	12.170	12.170	20.067
		F-20	5.3587	5.3587	9.0022	12.419	12.420	20.485
		F-27	5.3583	5.3583	9.0030	12.439	12.440	20.473
		F-35	5.3584	5.3584	9.0021	12.438	12.438	20.471
Lam et al. [7]			5.3583	5.3583	9.0732	12.439	12.439	20.521
Sato [4]			5.3592	5.3592	9.0120	—	—	—
Narita [5]			5.3583	5.3583	9.0031	12.439	12.439	20.475
Elliptic plate, $a/b = 2.0$								
LSFD	557	F-14	6.4458	9.9660	15.923	20.435	24.678	29.176
		F-20	6.6637	10.499	16.863	21.801	27.756	31.282
		F-27	6.6708	10.542	16.882	22.016	27.731	31.572
		F-35	6.6694	10.542	16.955	22.030	27.727	32.062
	1519	F-14	6.5993	10.321	16.604	21.356	26.656	30.692
		F-20	6.6687	10.536	16.910	21.967	27.778	31.478
		F-27	6.6705	10.547	16.918	22.011	27.772	31.505
		F-35	6.6705	10.547	16.922	22.015	27.758	31.538
	2504	F-14	6.6272	10.413	16.729	21.620	27.058	31.004
		F-20	6.6698	10.543	16.917	21.996	27.772	31.497
		F-27	6.6712	10.548	16.921	22.023	27.796	31.559
		F-35	6.6705	10.547	16.922	22.015	27.765	31.521
Lam et al. [7]			6.6704	10.548	16.923	22.021	27.777	31.523
Sato [4]			6.6667	—	—	—	27.773	31.517
Narita [5]			6.6705	10.548	16.921	22.015	27.768	31.513

Table 2
LSFD solution for the first six frequencies of the completely free lifting-tab shaped plate ($\Omega = \omega a^2\sqrt{\rho h/D}$, $v = 0.3$)

Method	Mesh	Formulation	Mode sequence					
			4th	5th	6th	7th	8th	9th
LSFD	1100	F-14	2.8132	3.8245	6.3050	7.9499	8.4411	11.966
		F-20	2.8493	3.9242	6.5292	8.2420	8.6937	12.455
		F-27	2.8425	3.9151	6.5299	8.2272	8.6916	12.512
	2067	F-14	2.8231	3.8600	6.3992	8.0440	8.5616	12.183
		F-20	2.8382	3.9061	6.5154	8.1908	8.6817	12.448
		F-27	2.8343	3.8974	6.5056	8.1680	8.6779	12.458
	3196	F-14	2.8307	3.8807	6.4375	8.1184	8.6079	12.281
		F-20	2.8361	3.9091	6.5084	8.2008	8.6764	12.440
		F-27	2.8306	3.9082	6.5045	8.1902	8.6772	12.438

Table 3
LSFD solution for the first six frequencies of the completely free 45° right triangular plate ($\Omega = \omega a^2\sqrt{\rho h/D}$, $v = 0.3$)

Method	Mesh	Formulation	Mode sequence					
			4th	5th	6th	7th	8th	9th
LSFD	1100	F-14	17.077	26.667	45.076	46.332	68.076	80.949
		F-20	17.846	27.316	44.637	46.934	65.769	80.593
		F-27	18.639	28.502	45.160	48.403	69.046	82.199
	2662	F-14	17.743	27.392	45.403	46.832	68.016	81.135
		F-20	18.317	28.018	45.051	47.672	67.359	81.203
		F-27	18.841	28.805	45.350	48.900	70.640	83.100
	3563	F-14	18.029	27.751	45.300	47.176	68.084	81.318
		F-20	18.570	28.387	45.187	48.218	68.679	81.955
		F-27	18.777	28.724	45.352	48.808	70.268	83.018
Relative frequency ratios								
LSFD	3563	F-27	1	1.53	2.42	2.60	3.74	4.42
Leissa [3]			1	1.4	2.36	2.56	3.65	4.39

Table 4
Radii of nodal circles $\rho = r/a$ for a completely free circular plate ($v = 0.33$)

Sources	ρ for values of $(n, s)^*$ of				
	(0, 1)	(1, 1)	(2, 1)	(0, 2)	(3, 1)
LSFD	0.6794	0.7807	0.8223	0.8406, 0.3904	0.8463
Leissa [3]	0.680	0.781	0.822	0.841, 0.391	0.847

$^*n$ is the number of nodal diameters, s is the number of nodal circles.

have very high accuracy when $N = 27$. It should be pointed out that the comparison study cannot be performed for the results of lifting-tab shaped plate as there are no exisiting data. In Table 3, the LSFD results for frequency parameters of the 45° right triangular plate are compared with experimentally obtained relative frequency ratios given in Leissa's book [3]. It can be seen that the agreement between the two sets of results is satisfactory. Note that for these two aforementioned plate shapes, the high accuracy of the LSFD results can be confirmed by the convergence behavior of the frequency values as shown in Tables 2 and 3. These two case studies demonstrate the capability of the LSFD method in solving PDEs with complex domains.

3.3.2. Mode shapes and modal stress resultants

The modal stress resultants for circular, elliptical, lifting-tab shaped and 45° right triangular plates are non-dimensionalized as follows: (1) in the plate domain, $\bar{M}_{x'} = M_{x'}a/D$, $\bar{M}_{y'} = M_{y'}a/D$ for the principal bending moments, $\bar{M}_{x''y''} = M_{x''y''}a/D$ for the maximum twisting moments, $\bar{Q}_{x'''} = |Q_{x'''}|a^2/D$ for the maximum absolute values of shear forces, and (2) at the plate edge, $\bar{M}_n = M_n a/D$ and $\bar{V}_n = V_n a^2/D$ for the normal bending moments and effective shear forces. All quantities are also normalized by setting $\bar{W}_{\max} = |W_{\max}/a| = 1$.

Table 4 shows the LSFD results for the radii of nodal circles of the five modes ($n = 0$, $s = 1$), ($n = 1$, $s = 1$), ($n = 2$, $s = 1$), ($n = 0$, $s = 2$) and ($n = 3$, $s = 1$) of the completely free circular plate, and they are compared with the benchmark data from Leissa [3]. The agreement between the two results is excellent.

The satisfaction of the boundary conditions $\bar{M}_n = 0$ and $\bar{V}_n = 0$ by LSFD solutions for the first four unrepeated modes, i.e., the 4th, 6th, 7th and 9th modes of the completely free circular plate, and the 4th to 7th modes of the completely free elliptical plate, lifting-tab shaped plate and 45° right triangular plate are examined by referring to Figs. 3–6 and Tables 5–8. Here we use Figs. 3–6 to show the error distributions of $\bar{M}_n$

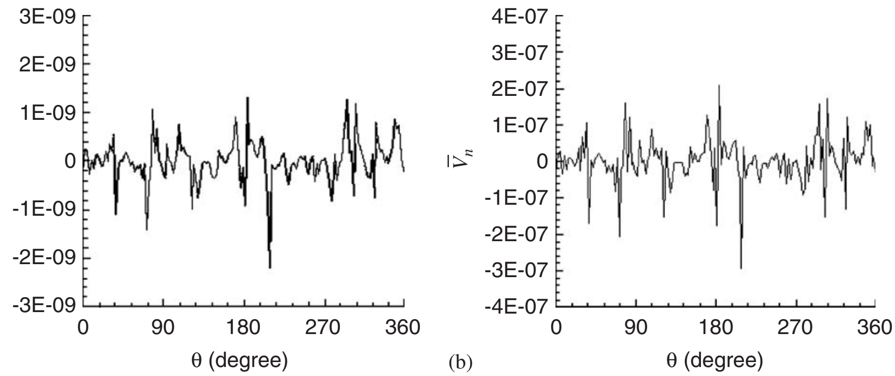

Fig. 3. Verification of natural boundary conditions $\bar{M}_n = 0$, $\bar{V}_n = 0$ for completely free circular plate vibrating in 4th mode.

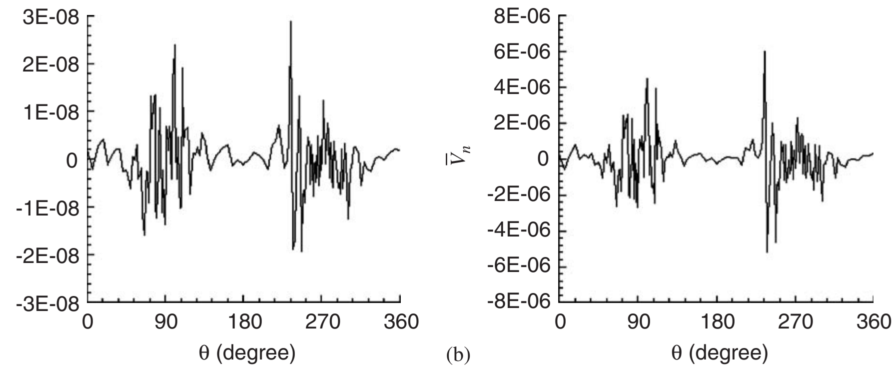

Fig. 4. Verification of boundary conditions $\bar{M}_n = 0$, $\bar{V}_n = 0$ for completely free elliptical plate ($a/b = 2$) vibrating in 4th mode.

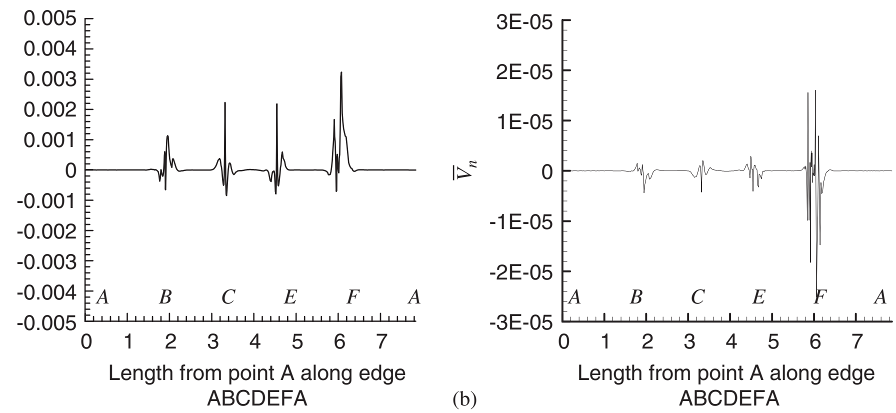

Fig. 5. Verification of boundary conditions $\bar{M}_n = 0$, $\bar{V}_n = 0$ for completely free lifting-tab shaped plate vibrating in 4th mode.

and $\bar{V}_n$ along the perimeter of the circular, elliptical, lifting-tab shaped and 45° right triangular plates, respectively, which are associated with the 4th mode. For the other three modes of these plates, the error distributions of $\bar{M}_n$ and $\bar{V}_n$ are similar to Figs. 3–6. It can be seen that the absolute errors and the relative errors (the values $(a)/(b)$ in Table 5) of $\bar{M}_n$ for the given four modes of the completely free circular plate are in the orders of 10^{-9} and 10^{-10}, respectively; and the absolute errors and the relative errors (the values $(c)/(d)$ in

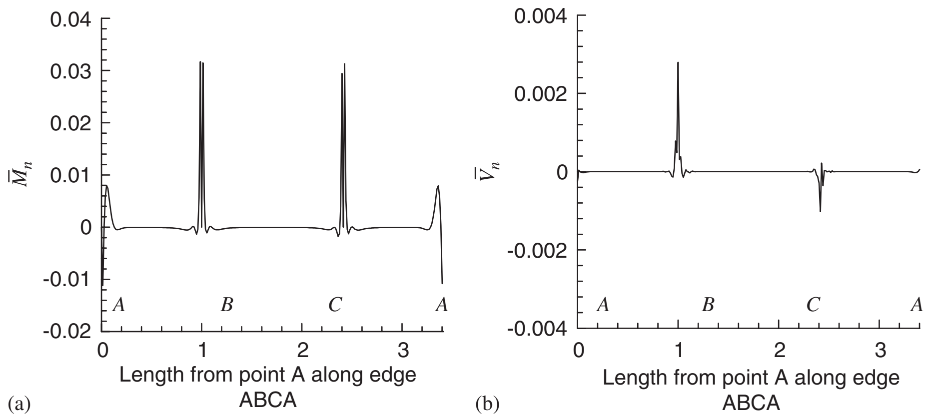

Fig. 6. Verification of boundary conditions $\bar{M}_n = 0,\ \bar{V}_n = 0$ for completely free 45° right triangular plate vibrating in 4th mode.

Table 5
Verification of boundary conditions $\bar{M}_n = 0$ and $\bar{V}_n = 0$ of the completely free circular plate ($\upsilon = 0.3$)

Mode	$\lvert\bar{M}_n\rvert_{\max}$ (a)	$\lvert\bar{M}_{x'}\rvert_{\max}$ (b)	(a)/(b)	$\lvert\bar{V}_n\rvert_{\max}$ (c)	$\lvert\bar{Q}_{x'''}\rvert_{\max}$ (d)	(c)/(d)
4th	2.2042×10^{-9}	2.2451	9.82×10^{-10}	2.9302×10^{-7}	4.2350	6.92×10^{-8}
6th	1.7963×10^{-9}	6.9502	2.58×10^{-10}	2.5015×10^{-7}	14.102	1.77×10^{-8}
7th	2.0890×10^{-9}	6.2950	3.32×10^{-10}	2.7744×10^{-7}	17.329	1.60×10^{-8}
9th	9.5366×10^{-10}	17.826	5.35×10^{-11}	9.7671×10^{-8}	84.775	1.20×10^{-9}

Table 6
Verification of boundary conditions $\bar{M}_n = 0$ and $\bar{V}_n = 0$ of the completely free elliptical plate ($a/b = 2$, $\upsilon = 0.3$)

Mode	$\lvert\bar{M}_n\rvert_{\max}$ (a)	$\lvert\bar{M}_{x'}\rvert_{\max}$ (b)	(a)/(b)	$\lvert\bar{V}_n\rvert_{\max}$ (c)	$\lvert\bar{Q}_{x'''}\rvert_{\max}$ (d)	(c)/(d)
4th	2.8835×10^{-8}	3.4342	8.40×10^{-9}	5.9902×10^{-6}	5.4731	1.09×10^{-6}
5th	5.1041×10^{-8}	4.3197	1.18×10^{-8}	9.4995×10^{-6}	12.293	7.72×10^{-7}
6th	2.4701×10^{-8}	7.6476	3.23×10^{-9}	5.2286×10^{-6}	25.754	2.03×10^{-7}
7th	4.2264×10^{-8}	11.336	3.73×10^{-9}	8.5711×10^{-6}	38.523	2.22×10^{-7}

Table 7
Verification of boundary conditions $\bar{M}_n = 0$ and $\bar{V}_n = 0$ of the completely free lifting-tab shaped plate (Fig. 2 Left, $\upsilon = 0.3$)

Mode	$\lvert\bar{M}_n\rvert_{\max}$ (a)	$\lvert\bar{M}_{x'}\rvert_{\max}$ (b)	(a)/(b)	$\lvert\bar{V}_n\rvert_{\max}$ (c)	$\lvert\bar{Q}_{x'''}\rvert_{\max}$ (d)	(c)/(d)
4th	3.2343×10^{-3}	1.3736	2.35×10^{-3}	2.5148×10^{-5}	1.4399	1.75×10^{-5}
5th	3.8864×10^{-2}	1.8244	2.13×10^{-2}	1.5011×10^{-3}	2.9322	5.12×10^{-4}
6th	5.4933×10^{-2}	3.2768	1.68×10^{-2}	1.1194×10^{-3}	6.1270	1.83×10^{-4}
7th	1.2546×10^{-1}	3.9402	3.18×10^{-2}	2.6513×10^{-3}	8.4088	3.15×10^{-4}

Table 5) of $\bar{V}_n$ are in the orders of 10^{-7} and 10^{-8}, respectively. For the completely free elliptical plate, the absolute errors and the relative errors (the values $(a)/(b)$ in Table 6) of $\bar{M}_n$ for the given four modes are in the orders of 10^{-8} and 10^{-9}, respectively. The absolute errors and relative errors (the values $(c)/(d)$ in Table 6) of $\bar{V}_n$ are in the orders of 10^{-6} and 10^{-7}, respectively. These errors are so small that we can think of the

satisfaction of the LSFD solutions to the free edge natural boundary conditions $\bar{M}_n = 0$ and $\bar{V}_n = 0$ as excellent. In sum, the LSFD solutions for the circular and elliptical plates are accurate and the modal stress resultants do satisfy the natural boundary conditions.

On the other hand, we find that the satisfaction of natural boundary conditions by the LSFD results for the lifting-tab shaped and 45° right triangular plates is not as good as that for the circular and elliptical plates. From Figs. 5 and 6, it is found that the errors of $\bar{M}_n$ and $\bar{V}_n$ pulsate at the vicinity of the four tangent points (denoted by letters B, C, E and F in Fig. 2a and in Fig. 5) on the edge curve of the lifting-tab shaped plate, and at the vicinity of the three corner vertices (denoted by letters A, B and C in Fig. 2b and Fig. 6) of the triangular plate. The amplitudes of these absolute and relative errors shown in Figs. 5 and 6 and Tables 7 and 8 can be regarded as small in engineering practices. Moreover, the natural boundary conditions are still strictly satisfied

Table 8
Verification of boundary conditions $\bar{M}_n = 0$ and $\bar{V}_n = 0$ of the completely free 45° right triangular plate (Fig. 2 Right, $v = 0.3$)

Mode	$\lvert\bar{M}_n\rvert_{\max}$ (a)	$\lvert\bar{M}_{x'}\rvert_{\max}$ (b)	(a)/(b)	$\lvert\bar{V}_n\rvert_{\max}$ (c)	$\lvert\bar{Q}_{x'''}\rvert_{\max}$ (d)	(c)/(d)
4th	3.1690×10^{-2}	8.2285	3.85×10^{-3}	2.7923×10^{-3}	16.149	1.73×10^{-4}
5th	7.9603×10^{-2}	11.334	7.02×10^{-3}	2.0756×10^{-2}	45.676	4.54×10^{-4}
6th	1.2427×10^{-1}	9.9135	1.25×10^{-2}	5.2472×10^{-3}	64.528	8.13×10^{-5}
7th	2.5993×10^{-1}	25.337	1.03×10^{-2}	3.4359×10^{-3}	117.97	2.91×10^{-5}

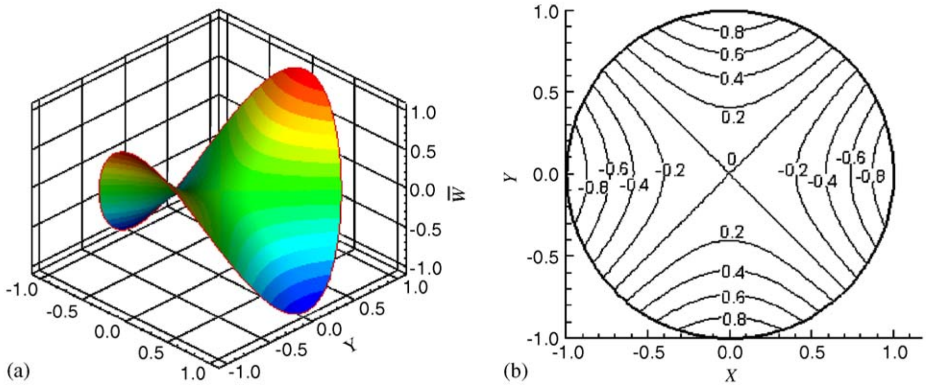

Fig. 7. Modal deflections $\bar{W}$ for circular plate vibrating in 4th mode.

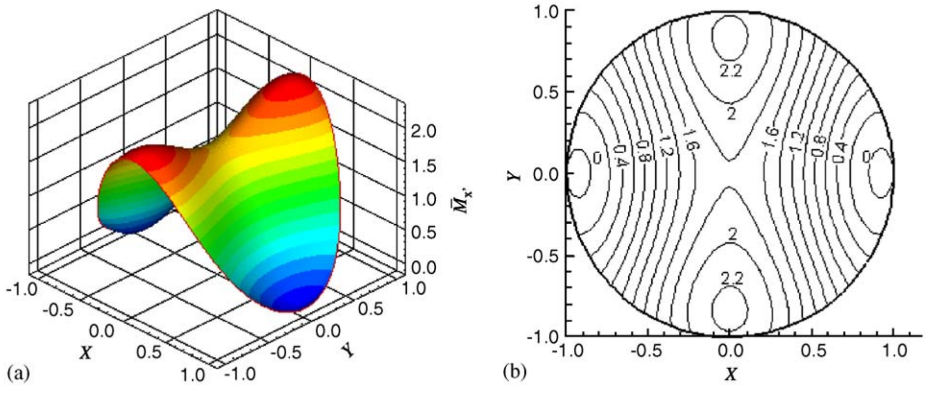

Fig. 8. First principal modal bending moments $\bar{M}_{x'}$ for circular plate vibrating in 4th mode.

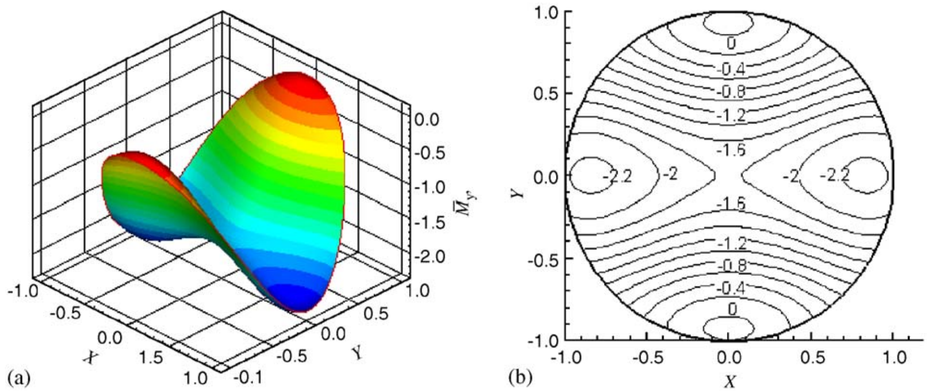

Fig. 9. Second principal modal bending moments $\bar{M}_{y'}$ for circular plate vibrating in 4th mode.

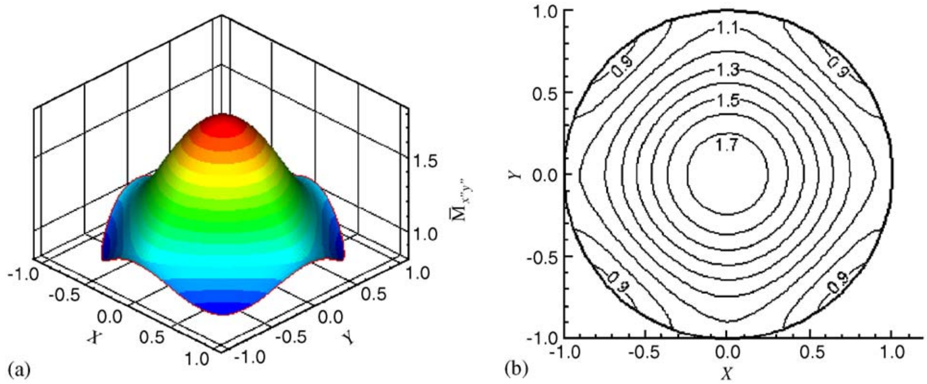

Fig. 10. Maximum modal twisting moments $\bar{M}_{x''y''}$ for circular plate vibrating in 4th mode.

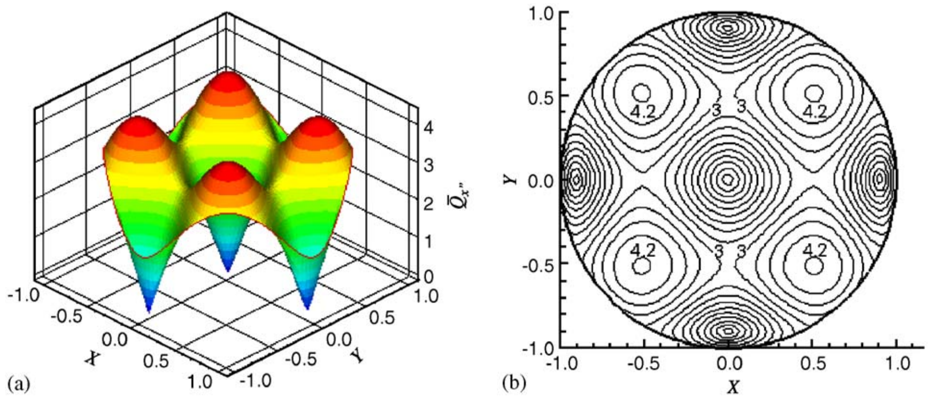

Fig. 11. Maximum modal shear forces $\bar{Q}_{x'''}$ for circular plate vibrating in 4th mode.

along a major portion of the plate edges. In sum, the numerical vibration characteristics of these two plates are actually not contaminated by these localized errors with small amplitudes.

The mode shapes and modal stress resultants for the fundamental modes of these four plates are presented in Figs. 7–26 in the forms of 3D displays and contour plots. Very good smoothness in the distributions of the

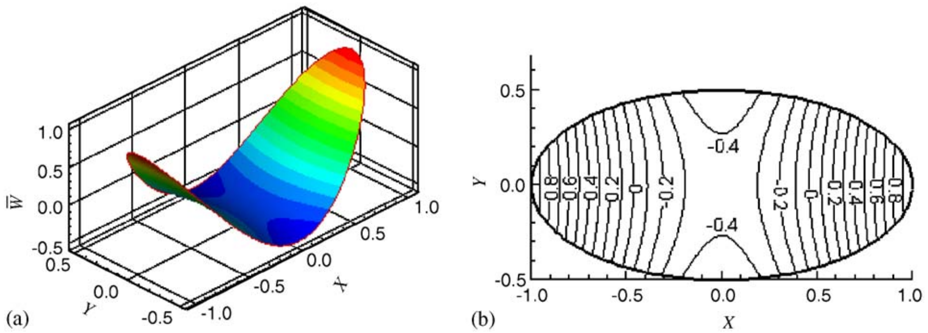

Fig. 12. Modal deflections $\bar{W}$ for elliptical plate ($a/b = 2$) vibrating in 4th mode.

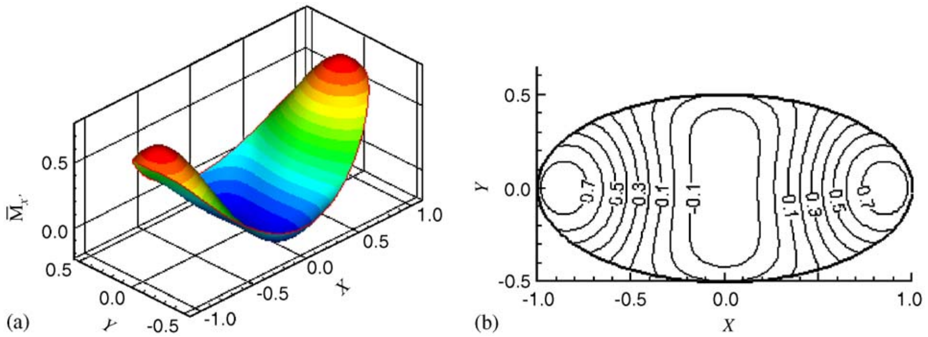

Fig. 13. First principal modal bending moments $\bar{M}_{x'}$ for elliptical plate ($a/b = 2$) vibrating in 4th mode.

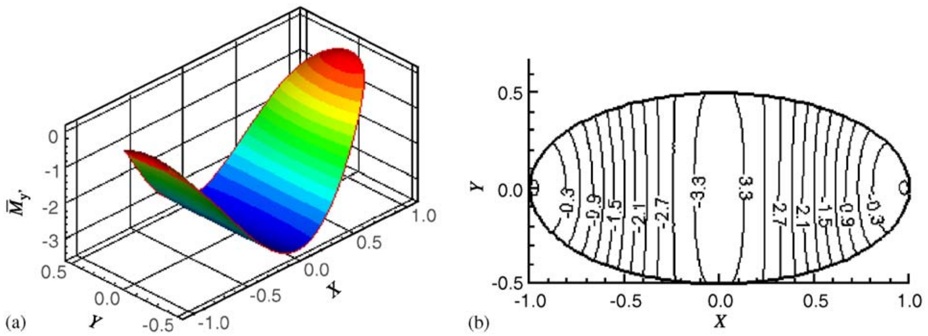

Fig. 14. Second principal modal bending moments $\bar{M}_{y'}$ for elliptical plate ($a/b = 2$) vibrating in 4th mode.

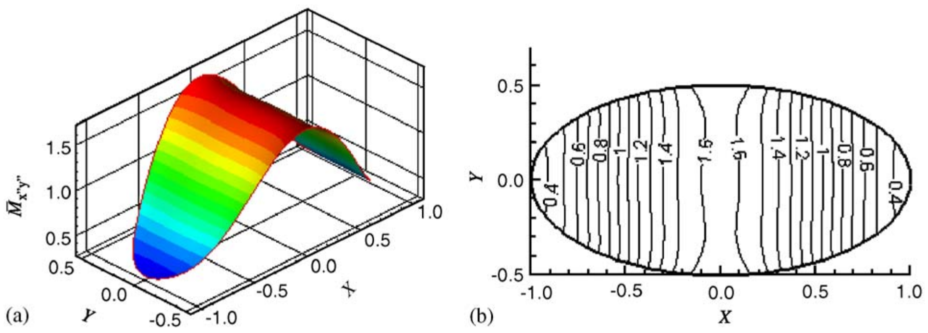

Fig. 15. Maximum modal twisting moments $\bar{M}_{x''y''}$ for elliptical plate ($a/b = 2$) vibrating in 4th mode.

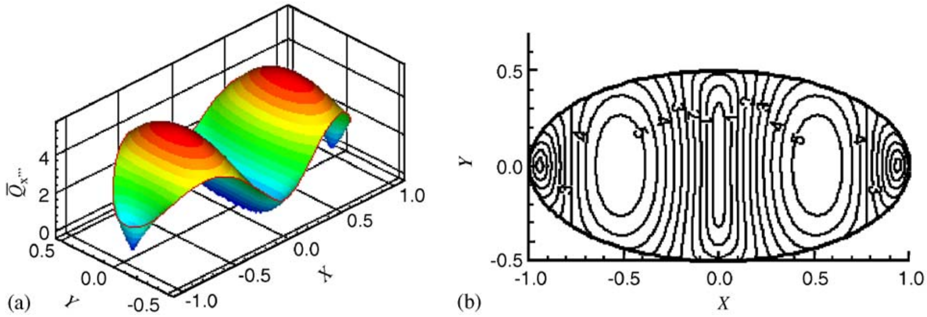

Fig. 16. Maximum modal shear forces $\bar{Q}_{x'''}$ for elliptical plate ($a/b = 2$) vibrating in 4th mode.

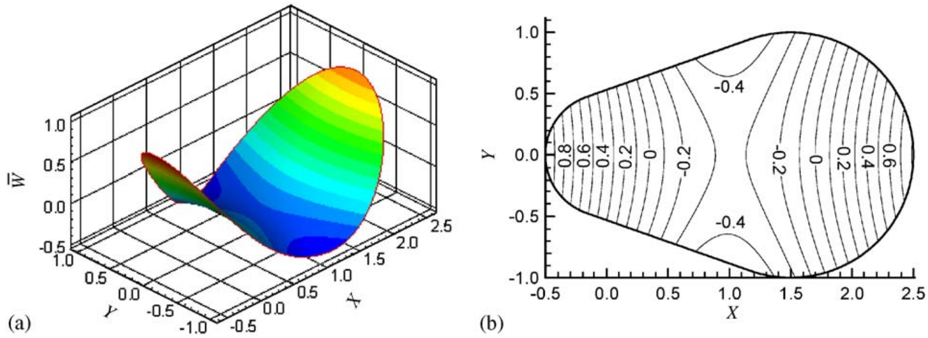

Fig. 17. Modal deflections $\bar{W}$ for lifting-tab shaped plate vibrating in 4th mode.

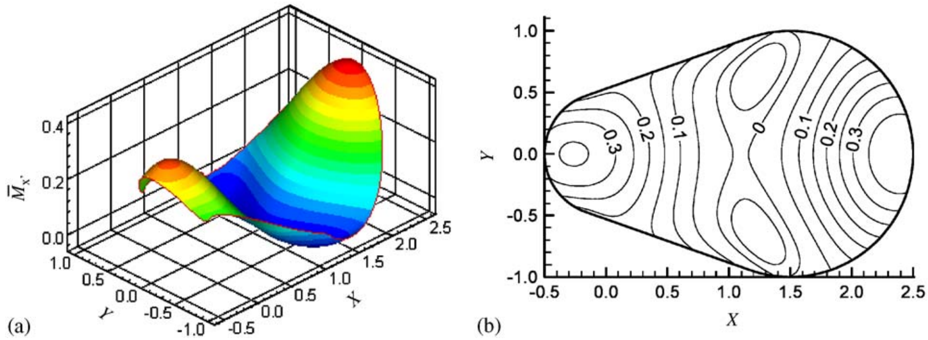

Fig. 18. First principal modal bending moments $\bar{M}_{x'}$ for lifting-tab shaped plate vibrating in 4th mode.

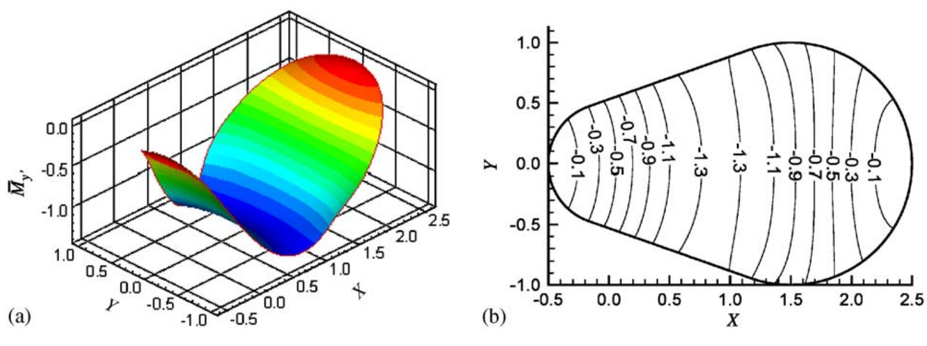

Fig. 19. Second principal modal bending moments $\bar{M}_{y'}$ for lifting-tab shaped plate vibrating in 4th mode.

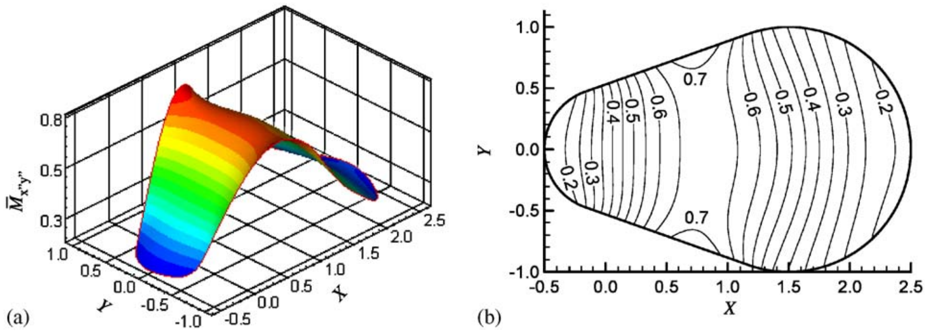

Fig. 20. Maximum modal twisting moments $\bar{M}_{x''y''}$ for lifting-tab shaped plate vibrating in 4th mode.

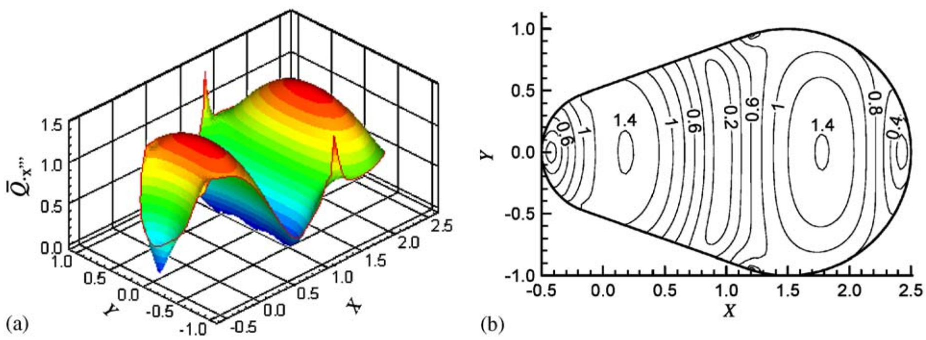

Fig. 21. Maximum modal shear forces $\bar{Q}_{x'''}$ for lifting-tab shaped plate vibrating in 4th mode.

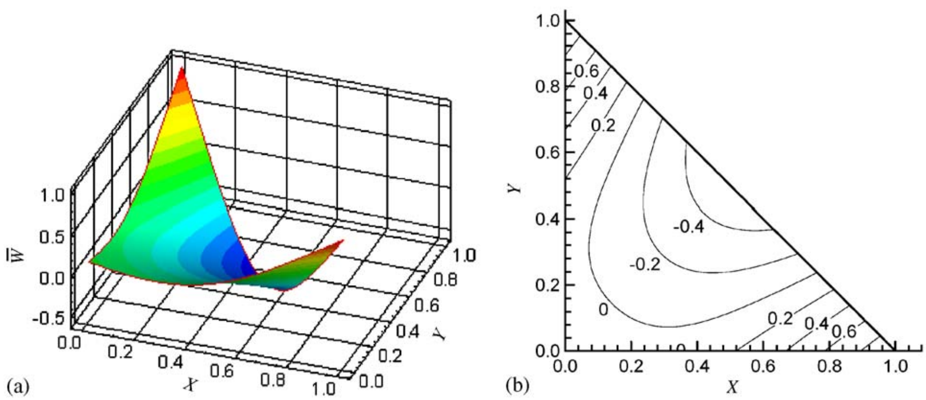

Fig. 22. Modal deflections $\bar{W}$ for 45° right triangular plate vibrating in 4th mode.

stress resultants can be observed from these 3D views, which further confirm the accuracy of the LSFD solutions for modal stress resultants.

The peak values of modal deflections and stress resultants as well as their locations in the completely free vibrating circular, elliptical, lifting-tab shaped and 45° right triangular plates are summarized in Tables 9–12. From the data in these tables, together with the 3D views and contour plots in Figs. 7–26, one can observe the details of the distributions of the modal stress resultants for the given modes of these completely free vibrating plates.

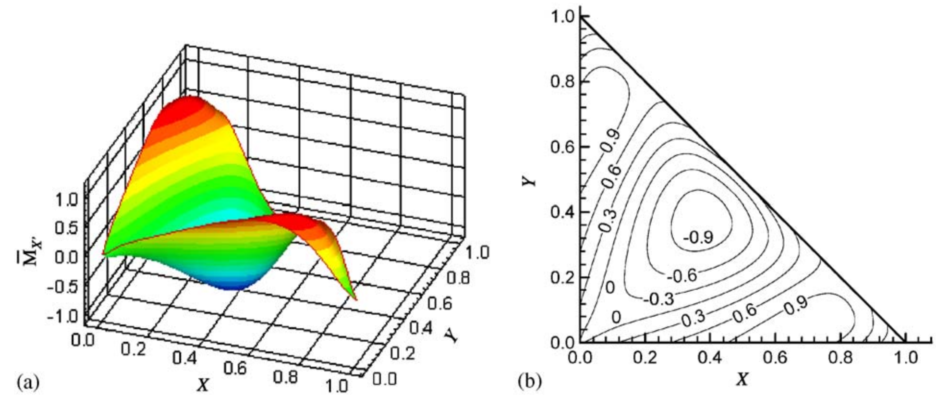

Fig. 23. First principal modal bending moments $\bar{M}_{x'}$ for 45° right triangular plate vibrating in 4th mode.

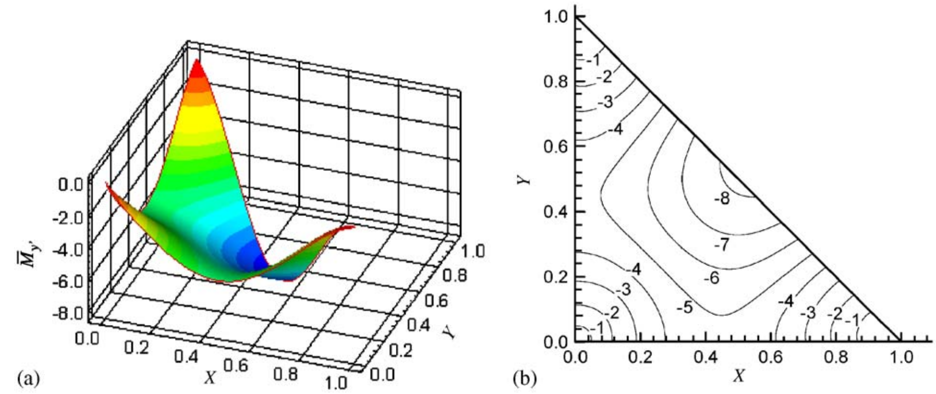

Fig. 24. Second principal modal bending moments $\bar{M}_{y'}$ for 45° right triangular plate vibrating in 4th mode.

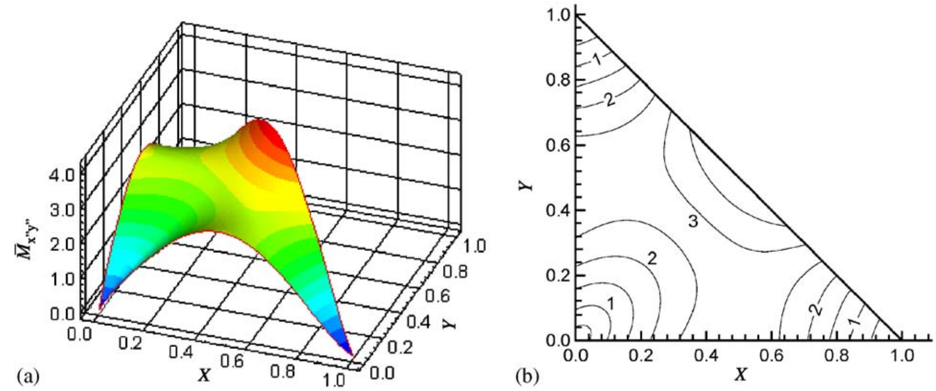

Fig. 25. Maximum modal twisting moments $\bar{M}_{x''y''}$ for 45° right triangular plate vibrating in 4th mode.

4. Conclusions

In this study, the recently developed LSFD meshfree method has been successfully applied for solving vibration problems of circular, elliptical, lifting-tab shaped and 45° right triangular plates with free edges. It is

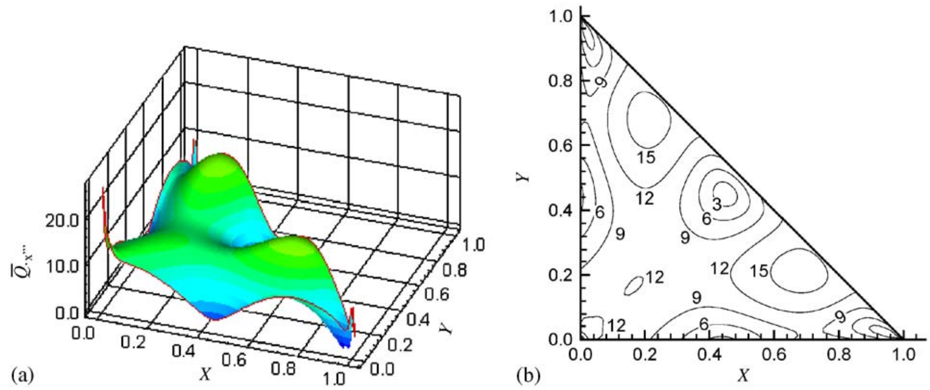

Fig. 26. Maximum modal shear forces $\bar{Q}_{x'''}$ for 45° right triangular plate vibrating in 4th mode.

Table 9
Peak values and corresponding locations of modal displacements $\bar{W}$, modal principal bending moments $\bar{M}_{x'}$ and $\bar{M}_{y'}$, maximum modal twisting moments $\bar{M}_{x''y''}$ and maximum modal shear forces $\bar{Q}_{x'''}$ for completely free circular plate ($v = 0.3$)

	Mode			
	4th	6th	7th	9th
$\bar{W}_{\max}$	1	1	1	1
r/a	1	0	1	1
$\bar{W}_{\min}$	−1	−0.7424	−1	−1
r/a	1	1	1	1
$\bar{M}_{x'}$	2.2451	6.9502	6.2950	17.826
r/a	0.8268	0	0.9629	0.4197
$\bar{M}_{y'}$	−2.2443	6.9489	−6.3019	−17.807
r/a	0.8600	0	0.9666	0.4080
$\bar{M}_{x''y''}$	1.7916	1.1615	3.1378	4.8585
r/a	0	0.8420	1	0.5312
$\bar{Q}_{x'''}$	4.2350	14.102	17.329	84.775
r/a	0.7212	0.5380	0.8219	0

Table 10
Peak values and corresponding locations of modal displacements $\bar{W}$, modal principal bending moments $\bar{M}_{x'}$ and $\bar{M}_{y'}$, maximum modal twisting moments $\bar{M}_{x''y''}$ and maximum modal shear forces $\bar{Q}_{x'''}$ for completely free elliptical plate ($a/b = 2$, $v = 0.3$)

	Mode			
	4th	5th	6th	7th
$\bar{W}_{\max}$	1	1	1	1
(X, Y)	(±1, 0)	(−0.64, −0.38) (0.64, 0.38)	(−1, 0)	(±0.79, −0.31)
$\bar{W}_{\min}$	−0.4836	−1	−1	−1
(X, Y)	(0, ±0.5)	(−0.64, 0.38) (0.64, −0.38)	(1, 0)	(±0.79, 0.31)
$\bar{M}_{x'}$	0.7699	4.3197	7.6471	11.334
(X, Y)	(±0.86, 0)	(0.39, 0.38), (−0.39, −0.38)	(0.43, ±0.44)	(0, 0.5)
$\bar{M}_{y'}$	−3.4342	−4.3188	−7.6476	−11.336
(X, Y)	(0, 0)	(−0.39, 0.38) (0.39, −0.38)	(−0.44, ±0.44)	(0, −0.5)
$\bar{M}_{x''y''}$	1.6665	3.6687	3.8424	6.3295
(X, Y)	(0, ±0.5)	(0, 0)	(±0.46, ±0.44)	(±0.48, 0)
$\bar{Q}_{x'''}$	5.4731	12.293	25.754	38.523
(X, Y)	(±0.53, 0)	(±0.60, 0)	(0, ±0.11)	(±0.79, 0)

Table 11
Peak values and corresponding locations of modal displacements $\bar{W}$, modal principal bending moments $\bar{M}_{x'}$ and $\bar{M}_{y'}$, maximum modal twisting moments $\bar{M}_{x''y''}$ and maximum modal shear forces $\bar{Q}_{x'''}$ for completely free lifting-tab shaped plate (Fig. 2 Left, $v = 0.3$)

	Mode			
	4th	5th	6th	7th
$\bar{W}_{max}$	1	1	1	1
(X, Y)	(−0.5, 0)	(0.14, −0.58)	(1.64, ±0.99)	(−0.20, −0.46)
$\bar{W}_{min}$	−0.4796	−1	−0.7959	−1
(X, Y)	(1.06, ±0.90)	(0.14, 0.58)	(2.5, 0)	(−0.20, 0.46)
$\bar{M}_{x'}$	0.4022	1.8144	2.1877	3.9269
(X, Y)	(2.42, 0)	(0.56, −0.73)	(1.67, ±0.91)	(1.05, 0.90)
$\bar{M}_{y'}$	−1.3719	−1.8244	−3.2768	−3.6443
(X, Y)	(0.79, ±0.81)	(0.57, 0.73)	(0.37, ±0.66)	(0.06, 0.55)
$\bar{M}_{x''y''}$	0.7322	1.2925	1.7638	2.2865
(X, Y)	(0.75, ±0.79)	(1.14, 0)	(1.77, 0)	(0.20, ±0.60)
$\bar{Q}_{x'''}$	1.4130	2.9322	6.1269	8.4088
(X, Y)	(0.19, 0)	(0.26, 0)	(1.12, ±0.58)	(−0.14, 0)

Table 12
Peak values and corresponding locations of modal displacements $\bar{W}$, modal principal bending moments $\bar{M}_{x'}$ and $\bar{M}_{y'}$, maximum modal twisting moments $\bar{M}_{x''y''}$ and maximum modal shear forces $\bar{Q}_{x'''}$ for completely free 45° right triangular plate (Fig. 2 Right, $v = 0.3$)

	Mode			
	4th	5th	6th	7th
$\bar{W}_{max}$	1	1	1	1
(X, Y)	(1, 0), (0, 1)	(1, 0)	(0, 0)	(1, 0)
$\bar{W}_{min}$	−0.5529	−1	−0.5411	−1
(X, Y)	(0.5, 0.5)	(0, 1)	(0.55, 0) (0, 0.55)	(0, 1)
$\bar{M}_{x'}$	1.1359	11.325	9.9135	25.337
(X, Y)	(0.04, 0.70)(0.70, 0.04)	(0, 0.48)	(0.11, 0.11)	(0.32, 0.68)
$\bar{M}_{y'}$	−8.2285	−11.334	−17.003	−25.337
(X, Y)	(0.5, 0.5)	(0.47, 0)	(0.49, 0) (0, 0.49)	(0.68, 0.32)
$\bar{M}_{x''y''}$	4.1144	5.8294	9.7100	13.176
(X, Y)	(0.5, 0.5)	(0.49, 0) (0, 0.49)	(0.40, 0) (0, 0.40)	(0.35, 0.65) (0.65, 0.35)
$\bar{Q}_{x'''}$	16.149	45.676	64.528	117.97
(X, Y)	(0.68, 0.21) (0.21, 0.68)	(0.21, 0.21)	(0.26, 0.06) (0.06, 0.26)	(0.47, 0.47)

shown that the LSFD method can be efficiently used to solve high-order PDEs with multiple boundary conditions. High-order derivatives can be approximated by using the LSFD formulations and the chain rule of discretization. The LSFD formulations for approximating derivatives in terms of local *nt*-coordinate system at boundary are proposed as an alternative way to discretize the boundary condition equations in which the derivatives are given in terms of local *nt*-coordinate system. The fourth-order governing PDE for free vibration of thin isotropic plates is discretized in two steps in which the first step reduces the fourth-order PDE to a second-order PDE and the second step reduces the second-order PDE to an algebraic equation. The two boundary conditions are implemented by solving the discretized PDEs for the boundary conditions of the free edge and then coupling with the discretized governing PDE.

The efficiency of the LSFD method was established with the yielding of not only accurate frequency parameters and mode shapes, but also accurate modal stress resultants for these completely free plates. It should be pointed out that the accurate stress resultants presented for these completely free vibrating plates are new, and they should be useful as reference solutions for VLFS engineers.

References

[1] E. Watanabe, C.M. Wang, T. Utsunomiya, T. Moan, Very large floating structures: applications, analysis and design, CORE Report No. 2004-02, Centre for Offshore Research and Engineering, National University of Singapore, 2004.

[2] K. Itao, S.H. Crandall, Natural modes and natural frequencies of uniform, circular, free-edge plates, ASME, *Journal of Applied Mechanics* 46 (1979) 448–453.

[3] A.W. Leissa, *Vibration of Plates (NASA SP 160)*, Government Printing Office, Washington, DC, US, 1969.

[4] K. Sato, Free flexural vibration of an elliptical plate with free edge, *Journal of the Acoustical Society of America* 54 (1973) 547–550.

[5] Y. Narita, Natural frequencies of free, orthotropic elliptical plates, *Journal of Sound and Vibration* 100 (1985) 83–89.

[6] C.S. Kim, S.M. Dickinson, On the lateral vibration of thin annular and circular composite plates subject to certain complicating effects, *Journal of Sound and Vibration* 130 (1989) 363–377.

[7] K.Y. Lam, K.M. Liew, S.T. Chow, Use of two-dimensional orthogonal polynomials for vibration analysis of circular and elliptical plates, *Journal of Sound and Vibration* 154 (2) (1992) 261–269.

[8] D.P. Beres, Vibration analysis of a completely free elliptical plate, *Journal of Sound and Vibration* 34 (1974) 441–442.

[9] D.J. Gorman, Free vibration analysis of the completely free rectangular plate by the method of superposition, *Journal of Sound and Vibration* 57 (1978) 437–447.

[10] D.J. Gorman, *Free Vibration Analysis of Rectangular Plates*, Elsevier, North Holland, New York, 1982.

[11] N. Li, The reciprocal theorem method for the free vibration analysis of plates: the completely free plate, *Journal of Sound and Vibration* 157 (2) (1992) 357–364.

[12] G.M. Oosterhout, P.J.M. van der Hoogt, R.M.E.J. Spiering, Accurate calculation methods for natural frequencies of plates with special attention to the higher modes, *Journal of Sound and Vibration* 183 (1) (1995) 33–47.

[13] Waller, D. Mary, Vibrations of free plates: isosceles right-angled triangles, *Proceedings of the Physical Society* 53 (part 1) (1941) 35–39.

[14] Waller, D. Mary, Vibrations of free plates, line symmetry, corresponding modes, *Proceedings of the Royal Society of London series A* 211 (1952) 265–276.

[15] T. Irie, G. Yamada, S. Aomura, Natural frequencies of Mindlin circular plates, *Transaction of ASME, Journal of Applied Mechanics* 47 (1980) 652–655.

[16] K.M. Liew, C.M. Wang, Y. Xiang, S. Kitipornchai, *Vibration of Mindlin Plates: Programming the p-Version Ritz Method*, Elsevier Science, Oxford, UK, 1998.

[17] C.M. Wang, Y. Xiang, E. Watanabe, T. Utsunomiya, Mode shapes and stress-resultants of circular Mindlin plates with free edges, *Journal of Sound and Vibration* 276 (2004) 511–525.

[18] C.M. Wang, T. Utsunomiya, E. Watanabe, On obtaining accurate stress resultants in vibration analysis of floating plate structures, *Journal of The Institution of Engineers, Singapore* 40 (5) (2000) 31–42.

[19] C.M. Wang, Y. Xiang, T. Utsunomiya, E. Watanabe, Evalution of modal stress resultants in freely vibrating plates, *International Journal of Solids and Structures* 38 (2001) 6525–6558.

[20] H. Ding, C. Shu, K.S. Yeo, D. Xu, Development of least square-based two-dimensional finite difference schemes and their application to simulate natural convection in a cavity, *Computers & Fluids* 33 (2004) 137–154.

[21] S.P. Timoshenko, S. Woinowsky-Krieger, *Theory of Plates and Shells*, McGraw-Hill, New York, 1959.